PAPER

Check for updates

Scale-up experiments of SO$_2$ removal and the promoting behavior of NO in moving beds at medium temperatures

Shuangchen Ma, [ID] *[ab] Xuan Bie,[ab] Chunqin Gong,[a] Baozhong Qu[a] and Daokuan Liu[a]

The dry flue gas desulfurization (FGD) method was studied, which is a part of the integrated removal of multi-pollutants at medium temperatures. Although dry flue gas treatment is a simple and effective method, it is still a highly empirical-led application technology. A superior desulfurization adsorbent, fine powder of NaHCO$_3$ (hereinafter called fine NaHCO$_3$), was selected by scale-up experiments. A deep understanding of the reaction process and mechanism is then explored, which helps the further optimization of dry desulfurization. Based on the multi-factor experiments for NaHCO$_3$, the effect mechanism of NO on desulfurization using NaHCO$_3$ is also proposed. The conversion of SO$_3^{2-}$ → SO$_4^{2-}$ is promoted by the existence of NO. Therefore, a slight decline can be found. According to the influences of the SO$_2$ concentration and the residence time, it is concluded that the diffusion of SO$_2$ into the channel of NaHCO$_3$ is the rate-limiting step. Impressively, the reaction process of reactants was clearly studied by *in situ* FTIR spectroscopy to determine the whole process. Moreover, the recycling of NaHCO$_3$ is the main direction for reducing adsorbent consumption in the next step. The predictable insights are beneficial for profoundly understanding the gas composition synergetic interaction for the SO$_2$ removal by the dry treatment using NaHCO$_3$.

1 Introduction

The combustion of fossil fuels (*e.g.*, coal, petroleum, flammable gases, *etc.*) is widely used for human activities and in industries,[1–3] which cause the generation of gas pollutants such as sulfur dioxide, nitrogen oxides, particulate matters, heavy metals, and organic matter.[4–10] Limestone-based wet flue gas desulfurization (Ca-WFGD) and ammonia-based selective catalytic reduction (NH$_3$-SCR) denitrification are simultaneously used in the pollutant control system in power plants.[10–12] However, huge investment and operating costs, complicated system and secondary pollution have attracted considerable attention.[13,14] Dry simultaneous control technologies are promisingly investigated without large water assumptions and low secondary pollution.[15–27]

Among the dry integrated multi-pollutant removal technologies, the carbon-based catalyst-integrated removal technology was widely studied,[28,29] particularly in the sintering flue gas industry.[30] Activated coke/activated carbon is used as a dry adsorbent. The adsorption tower is placed downstream of the precipitator. More than 98% SO$_2$ and sulfur trioxide (SO$_3$), 30% to 60% NO$_x$, 90% mercury and 50% particulate matter[31] will be captured in the system. The process involves three stages of adsorption, activated coke regeneration and by-product recovery, as shown in Fig. 1.

Besides, high-energy electron activation oxidation technologies[33–37] and photo-catalysis technologies have been attempted,[38–41] but these technologies are challenging to achieve high denitrification efficiency and lower the cost.

Under the condition of medium temperatures (200–500 °C) for the multi-pollutant integrated removal, the temperature zone is a suitable range for selective catalytic reduction (SCR), which is beneficial for the synergistic removal of SO$_2$ and NO$_x$. It has caused intense concerns in the industry. The schematic diagram of the integrated removal of multi-pollutants at the medium temperature zone is shown in Fig. 2. The integrated removal of multiple pollutants is realized by a single system. This broad market prospect system is more conducive to the comprehensive utilization of fly ash and owns the advantages of a high degree of system integration, a significant reduction in pollutant control costs, and no wastewater discharge.[42]

The adsorbents researched under medium-temperature conditions involve copper oxide (CuO), sodium bicarbonate (NaHCO$_3$), and calcium adsorbents. Most research studies concentrated on removing single pollutants or synergistically removing SO$_2$ and NO. However, most of them were experimental studies in a fixed bed, lacking research data on desulfurization in bench systems and moving beds.

[a]Hebei Key Lab of Power Plant Flue Gas Multi-Pollutants Control, Department of Environmental Science and Engineering, North China Electric Power University, Baoding, 071003, PR China. E-mail: msc1225@163.com; Fax: +86-312-7525521; Tel: +86-312-7525521

[b]MOE Key Laboratory of Resources and Environmental Systems Optimization, College of Environmental Science and Engineering, North China Electric Power University, Beijing, 102206, PR China
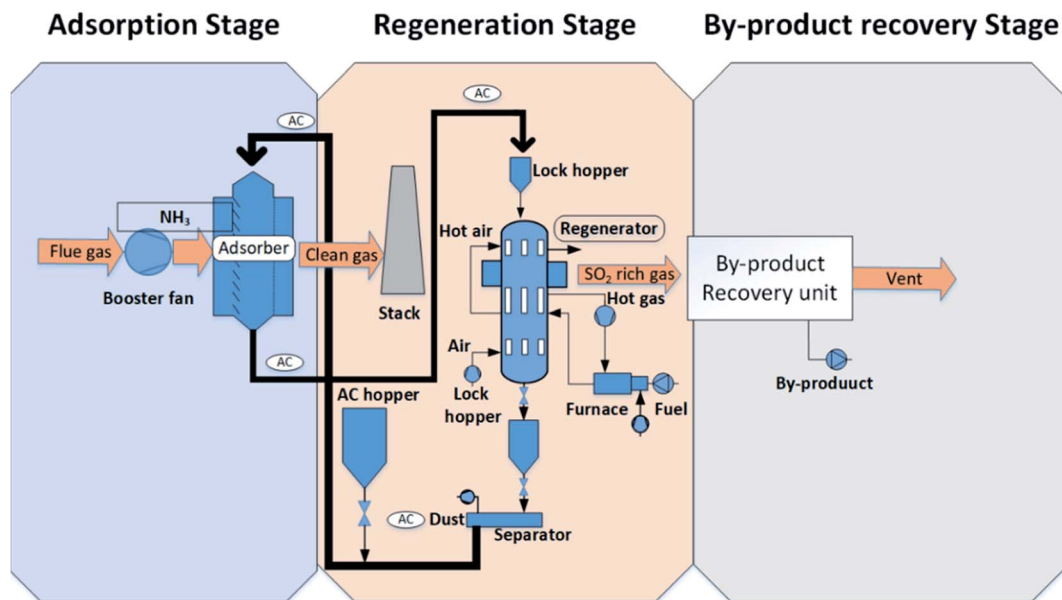
Fig. 1 Multi-pollutant integrated removal process using activated coke.[32]

Herein, we select the appropriate desulfurizer from different kinds of adsorbents and systematically reveal influences on dry desulfurization in scale-up experiments for flue injection to achieve multi-pollutant integrated removal. Surprisingly, a removal efficiency of more than 98% was achieved by fine $NaHCO_3$. It is worth mentioning that *in situ* FTIR spectroscopy was used to better integrate the influence mechanism in the removal process. Suitable desulfurization conditions for the bench system were discussed, which lays the foundation for the next step of SO_2, NO_x and dust removal in practical engineering applications.

2   Experimental method

2.1   Experimental device

Based on the moving bed reactor, the multi-pollutant integrated removal test bench was designed. The whole experimental system is shown in Fig. 3. Insulation cotton was used for keeping the temperature drop with a reasonable range constant in the reaction zone.

The simulated flue gas entered the heater after passing through the mixing device, and the simulated flue gas flow rate varied from 50 to 68 m^3 h^{-1}, depending on the specific situation. The flue gas was heated to the required temperature by the electric heating tube in the heater. Then, the flue gas entered the reaction zone. The feeding device was arranged at the heating zone outlet, and the entire feeding device was sealed. The feeding direction was perpendicular to the gas flow direction, ensuring uniform mixing of the feed and the flue gas. The whole reaction zone was 11.4 m in length, and the inner diameter of the reaction pipe section was 50 mm, which ensured sufficient reaction time.

The reacted flue gas entered the cyclone dust collector for dust removal, and then the induced air blower was used to provide power to the whole system. After the draft fan was induced, part of the flue gas was introduced into the flue gas analyzer to measure the flue gas component concentration following the reaction, and the rest of the flue gas was discharged into the atmosphere after the tail gas treatment. The temperature of the reaction zone was set
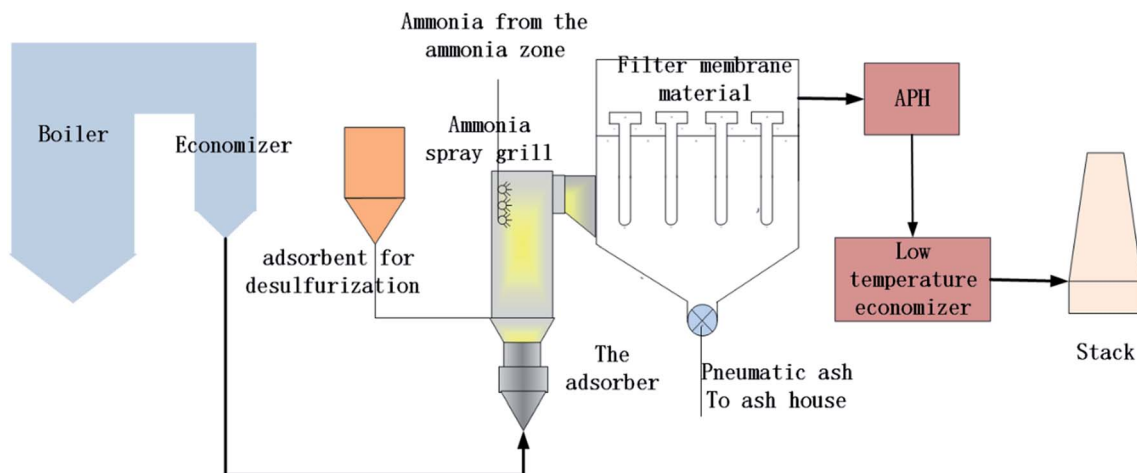

Fig. 2 Schematic diagram of the integrated removal of multi-pollutants at medium temperatures.
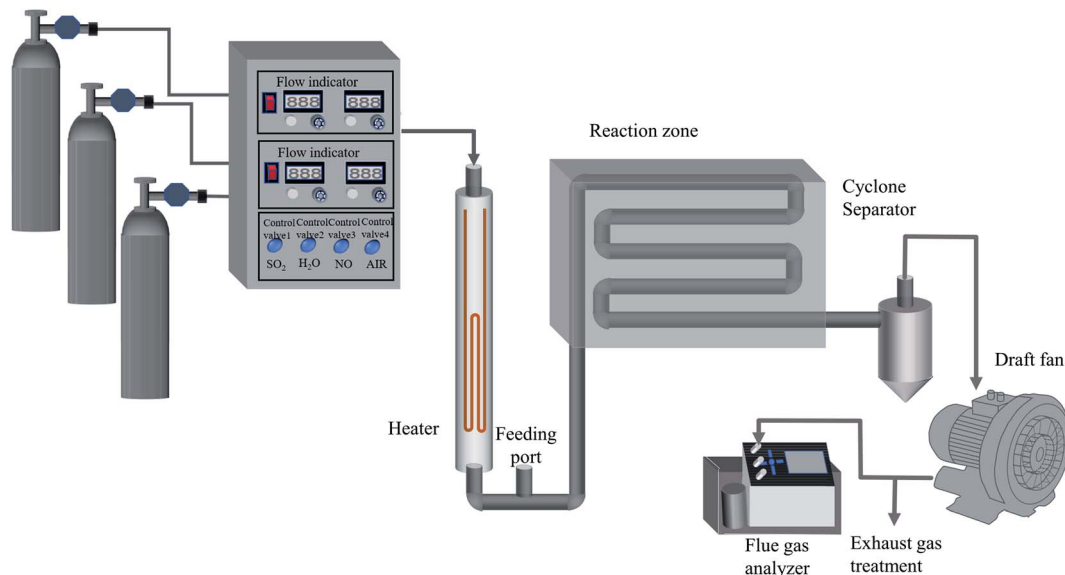
Fig. 3 Schematic diagram of the temperature desulfurization test bench.

at the desired temperature on the temperature control panel, and the flue gas flow was controlled by the flow controller.

2.2 SO$_2$ adsorption experiment

The simulated flue gas was a mixture of air, SO$_2$, NO, and so on. Pure SO$_2$ and air were mixed uniformly in the mixing device and the SO$_2$ concentration was controlled to achieve the required conditions. Pure NO was also mixed in the mixing device and the NO concentration was controlled to achieve the required condition. The water vapor was first generated by evaporation. In addition, its concentration was controlled by the knob. Then, it was introduced into the mixing device and then vaporized after heating. CO$_2$ was supplied directly from the cylinder and introduced into the mixing device. The draft fan powered the cycle of the entire process. The SO$_2$ removal efficiency was calculated in combination with the initial SO$_2$ concentration and that of the outlet. The adsorbents to be screened were: sodium carbonate (Na$_2$CO$_3$), sodium bicarbonate (NaHCO$_3$), magnesium hydroxide (Mg(OH)$_2$), magnesium oxide (MgO), and calcium hydroxide (Ca(OH)$_2$).

First, adsorbent screening was finished on the self-made experimental bench. Then, the one with the best performance was carried out to explore the SO$_2$ removal effect on different factors on the experimental bench.

The factors that needed to be explored were temperature, residence time, sodium-to-sulfur ratio, the particle size of the desulfurizer and flue gas composition. The flue gas components consisted of SO$_2$, CO$_2$, NO$_x$, water vapor and so on. The temperature was adjusted by the heating zone. The residence time was adjusted by the air volume of the experimental system. The sodium-to-sulfur ratio was adjusted by the amount of materials added, and the SO$_2$ concentration was controlled by the volume flow of SO$_2$ entering the air mixture device. NO$_x$, water vapor, CO$_2$, *etc.*, were respectively controlled by the flow meter. The particle size of the desulfurizer was adjusted by adsorbents of different particle sizes.

2.3 Product characterization experiment

X-ray diffraction (XRD) patterns were acquired using an X-ray diffractometer (D8 advance XRD diffractometer, Swiss Buker Company) between 10° and 90° at a rate of 10° min^{-1}. The thermogravimetric test was carried out using a Netzsch thermogravimetric analyzer under the flow of nitrogen at a heating rate of 10 °C min^{-1}. A BET analyzer was made by American Quantatech Co. The ion chromatograph was produced by Thermo. The particle size was measured using a NKT6100-B dry and wet integrated laser particle size analyzer manufactured by Shandong Nikeite Analytical Instrument Co., Ltd.

The *in situ* FTIR spectra were recorded using a Frontier FTIR Spectrometer, from PerkinElmer, USA. The instrument was equipped with a 10 cm demountable gas cell and a highly sensitive MCT detector. The total gas flow rate in the experiment was fixed at 200 mL min^{-1}. Two groups of FTIR experiments were carried out. Before each experiment, the samples were pretreated at 200 °C under the flow of N$_2$ (200 mL min^{-1}) for 30 min to remove physically adsorbed water, and then, the background spectra were recorded at 200 °C under N$_2$ flow, which should be deducted from the spectra of samples. Both samples in each group were investigated at 200 °C in a flow of required composition of the gas (200 mL min^{-1}) maintaining for demanded time, as shown in Table 1.

2.4 Parameter definition

For the sake of understanding a few special concepts, some parameters are defined as follows:

(1) Ratio of material to SO$_2$ (M/S): the ratio of the molar amount of the added material to the molar amount of SO$_2$. The following ratios of calcium to sulfur, sodium to sulfur, and magnesium to sulfur are collectively referred to as the ratio of material to sulfur. Their definitions are as follows.

Calcium-to-sulfur ratio (Ca/S): the molar amount of calcium hydroxide added to the reaction zone to the molar amount of sulfur dioxide in the flue gas;

Table 1 Test procedures for *in situ* FTIR spectroscopy

Test procedures for *in situ* FTIR	Conditions	
	Group 1	Group 2
Pretreatment	30 min with N_2	30 min with N_2
Step 1	20 min with 700×10^{-6} SO_2/N_2	20 min with 450×10^{-6} NO/N_2
N_2 purging	30 min with N_2	30 min with N_2
Step 2	20 min with 700×10^{-6} SO_2 + 21% O_2/N_2	20 min with 700×10^{-6} SO_2 + 450×10^{-6} NO/N_2
N_2 purging	30 min with N_2	30 min with N_2
Step 3	20 min with SO_2 + 21% O_2 + 8% H_2O (gas)/N_2	20 min with 700×10^{-6} SO_2 + 450×10^{-6} NO + 21% O_2/N_2
N_2 purging		30 min with N_2
Step 4		20 min with 700×10^{-6} SO_2/N_2

Sodium-to-sulfur ratio (Na2/S): the molar amount of sodium carbonate or half of sodium bicarbonate added to the reaction zone to the molar amount of sulfur dioxide in the flue gas;

Magnesium-to-sulfur ratio (Mg/S): the molar amount of magnesium oxide added to the reaction zone to the molar amount of sulfur dioxide in the flue gas.

(2) Theoretically, when Ca/S = 1 of calcium hydroxide, calcium hydroxide can be completely reacted with SO_2, like the magnesium oxide and sodium carbonate are. However, when $NaHCO_3$ is used, 1 mol can be completely reacted with 0.5 mol of SO_2. Therefore, Na2/S is introduced for $NaHCO_3$ to intuitively express the results.

(3) When calculating the desulfurization efficiency under different conditions, the desulfurization efficiency value in the stable range of desulfurization efficiency is used, and the desulfurization efficiency calculation formula is as follows:

$$\eta = \left(1 - \frac{\int_{t_1}^{t_2} \frac{(C_1 + C_2)Q}{2} \mathrm{d}t}{\int_{t_1}^{t_2} C_0 Q \mathrm{d}t} \right) \times 100\% \quad (1)$$

where η is the $Ca(OH)_2$ desulfurization efficiency; C_1 and C_2 are the actual concentrations measured by the flue gas analyzer at the moment of t_1 and t_2, respectively, mg m^{-3}; C_0 is the initial SO_2 concentration, mg m^{-3}; and Q is the mixed flue gas flow rate, L min^{-1}.

Because the flow rate of flue gas entering the flue gas analyzer is constant, formula (1) can be simplified as follows:

$$\eta = \left(1 - \frac{\frac{(C_1 + C_2)}{2}}{C_0} \right) \times 100\% \quad (2)$$

3 Results and discussions

3.1 Desulfurization effects for different adsorbents

Using a self-made experimental system, the adsorbents selected were $Mg(OH)_2$, MgO, Na_2CO_3, $NaHCO_3$ and $Ca(OH)_2$. The flue gas flow rate was controlled at 50 m^3 h^{-1}; the inlet SO_2 concentration was set as 2000 mg m^{-3}, and the desulfurization efficiency for different adsorbents at different temperatures is shown in Fig. 4.

As shown in Fig. 4, the best SO_2 removal efficiency is exhibited by $NaHCO_3$ at both 300 °C and 400 °C, followed by $Ca(OH)_2$, Na_2CO_3, MgO and $Mg(OH)_2$. Under any conditions, slight changes in the desulfurization efficiency by Na_2CO_3, MgO, $Mg(OH)_2$ are shown, while the removal efficiencies by $NaHCO_3$ and $Ca(OH)_2$ grow by the increased M/S ratio. Comparing the desulfurization efficiencies of the same materials at different temperatures, the desulfurization efficiency of $NaHCO_3$ presents a slight decrease through enhanced temperature, while the graph shows a sharp rise in the efficiency for $Ca(OH)_2$. At the same time, it was found that $Ca(OH)_2$, $Mg(OH)_2$ and MgO were easily adhesive to the pipe, which were very hygroscopic. However, $NaHCO_3$ exhibited better gas-phase spatial dispersion. According to the above-mentioned analysis, $NaHCO_3$ was selected as the optimum adsorbent to carry out the following experiments.

3.2 Influence of different flue gas compositions on SO_2 removal

Porous and highly active sodium carbonate is produced by decomposed $NaHCO_3$ above 50 °C, as shown in Fig. 5. This process is called the popcorn effect,[43] and a porous sponge-like structure is formed. SO_2 is diffused and adsorbed on the surface
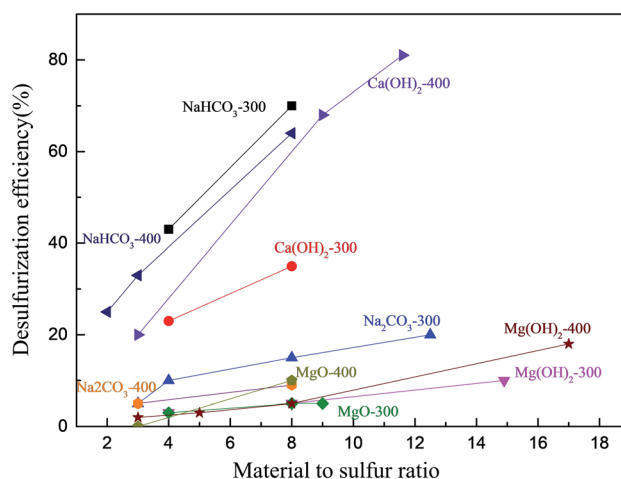

Fig. 4 Desulfurization efficiency for different adsorbents with temperature changing (the number on the label represents the temperature, °C).
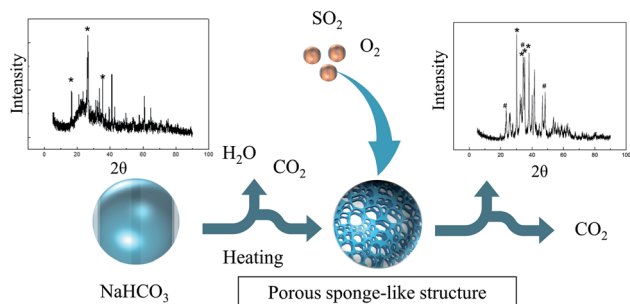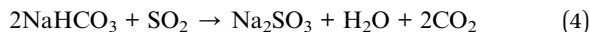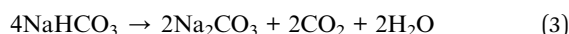
Fig. 5 Schematic of desulfurization using $NaHCO_3$ (where symbol * represents the characteristic peak of sodium carbonate and symbol # represents the characteristic peak of sodium sulfite).

of sodium carbonate. Compared with the diffraction peaks before the reaction, the crystal form changes after the reaction can be found, and the characteristic peaks of Na_2SO_3 appear.

The main reactions are listed as follows:

$$4NaHCO_3 \rightarrow 2Na_2CO_3 + 2CO_2 + 2H_2O \qquad (3)$$

$$2NaHCO_3 + SO_2 \rightarrow Na_2SO_3 + H_2O + 2CO_2 \qquad (4)$$

$$4NaHCO_3 + 2SO_2 + O_2 \rightarrow 2Na_2SO_4 + 4CO_2 + 2H_2O \qquad (5)$$

It can be seen from Fig. 6a that the efficiency is decreased with the increase in the concentration of CO_2. When the Na2/S is 2, the SO_2 removal efficiency is decreased from 30% to 22% at a concentration of CO_2 from 0 to 15%, and the SO_2 removal efficiency is reduced from 57% to 47% when the Na2/S is 4. The active sites in the porous sponge-like structure can be occupied by CO_2 diffused, thereby hindering the combination with SO_2. As shown in Fig. 6b, the removal efficiency is strengthened when water vapor is introduced into the pipe. When the Na2/S is 4, the SO_2 removal efficiency is expanded from 41.5% without water vapor to 70% containing water vapor. Similar trends are also demonstrated as the sodium-to-sulfur ratio is 2. More importantly, as shown in Fig. 6h and j, the amount of CO_3^{2-} remaining in the sample without water vapor is higher than that with water vapor. It is indicated that the amount of Na_2CO_3 remaining in the sulfated samples can be decreased by the addition of water vapor and the sulfation efficiency can be
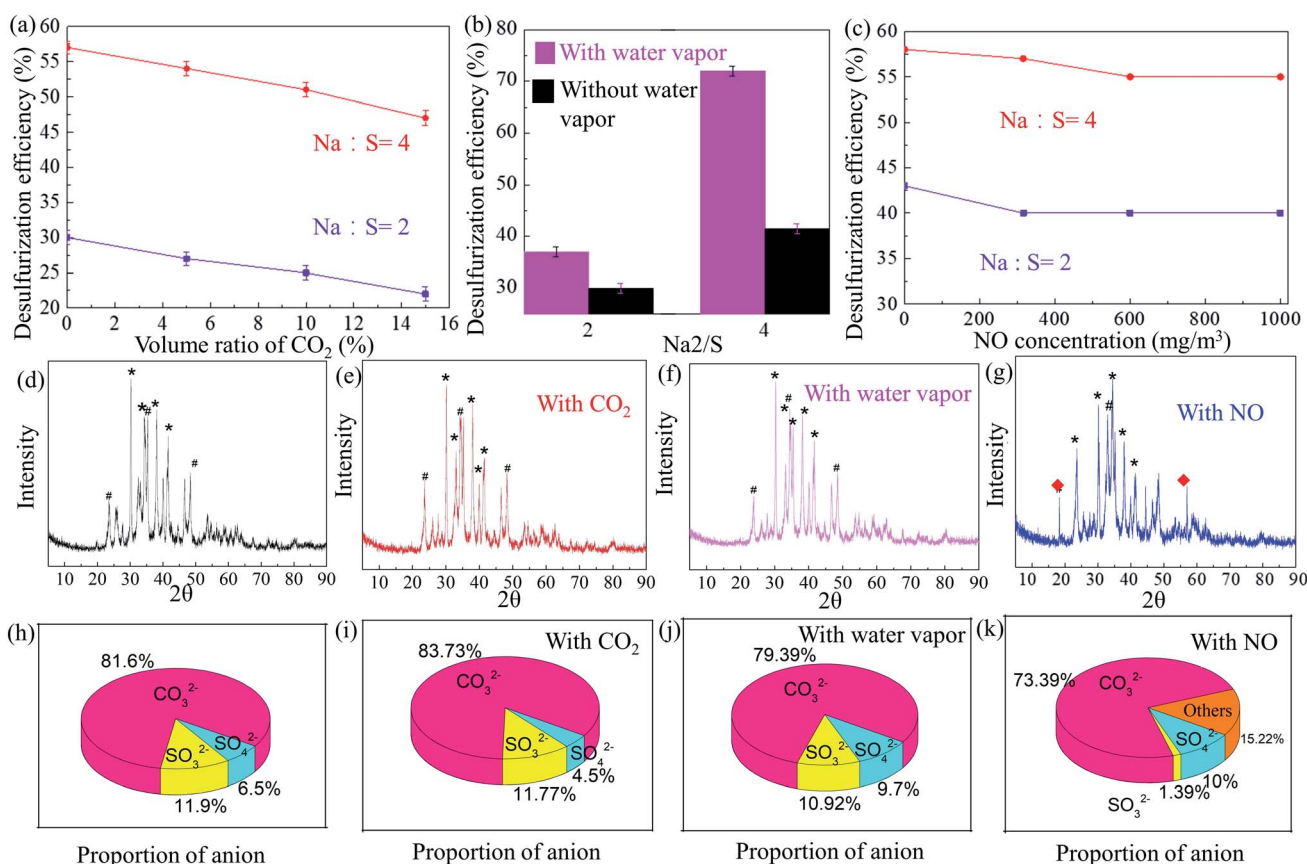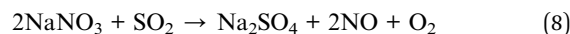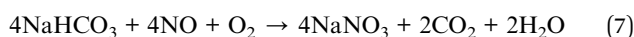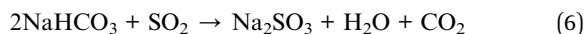

Fig. 6 (a) Effect of CO_2 on SO_2 removal. (b) Effect of water vapor on the removal of SO_2 (water vapor content: (1%)). (c) Effect of NO on SO_2 removal (NO concentration was 300 mg m^{-3}). (d) XRD results of the desulfurization product. (e) XRD results of the desulfurization product under a condition with CO_2. (f) XRD results of the desulfurization product under a condition with water vapor. (g) XRD results of the desulfurization product under a condition with NO. (h) Content of the desulfurization product. (i) Content of the desulfurization product under a condition with CO_2. (j) Content of the desulfurization product under a condition with water vapor. (k) Content of the desulfurization product under a condition with NO (where symbol * represents the characteristic peak of sodium carbonate and symbol # represents the characteristic peak of sodium sulfite) (temperature: inlet temperature of the reaction zone was 220 °C, the outlet temperature of the reaction zone was 180 °C; the air flow rate was 50 m^3 h^{-1}; Na2/S were 2 and 4 respectively; SO_2 concentration was 2000 mg m^{-3}).

improved when more Na_2CO_3 is utilized. Different hypotheses have been proposed around the influence mechanism of water vapor on calcination and sulfation recently.[44–49] One hypothesis[50] is that the solid-state diffusion can be enhanced by water vapor, which consolidates the calcination reaction rate. Herein, this hypothesis can be used to explain the results shown in Fig. 6h and j. The sulfation rate of Na_2CO_3 in the diffusion-controlled stage is enhanced by water vapor. Both the decomposition and sulfation reaction would be intensified by water vapor.

It can be seen from Fig. 6c that the desulfurization efficiency is decreased with the introduction of NO. The Fig. 6k reveals that the introduction of NO contributes to the formation of SO_4^{2-}. Interestingly, Fig. 6g reveals that no characteristic peak of NO_3^{2-} is observed, which is consistent with the phenomenon in other studies.[51] Hou *et al.*[51] found no NO_3^- was shown in the FTIR and XRD analyses as a result of low concentrations. He also found a higher desulfurization rate caused by NO. However, only a slight decline in the desulfurization rate is observed in our experiments. This may be caused by the production of nitrate or nitrite species. This can be proved by the appearance of other contents in Fig. 6k, which is determined later by *in situ* FTIR results. The facilitating effect of the conversion to sulfate was subsequently confirmed by *in situ* infrared characterization. According to the results, NO can be reacted with $NaHCO_3$, thereby inhibiting the reaction between SO_2 and $NaHCO_3$, while the conversion to SO_4^{2-} can be promoted by the formation of NO_3^-. The reaction in our hypothesis is as follows, which still needs further confirmation:

$$2NaHCO_3 + SO_2 \rightarrow Na_2SO_3 + H_2O + CO_2 \quad (6)$$

$$4NaHCO_3 + 4NO + O_2 \rightarrow 4NaNO_3 + 2CO_2 + 2H_2O \quad (7)$$

$$2NaNO_3 + SO_2 \rightarrow Na_2SO_4 + 2NO + O_2 \quad (8)$$

Notably, in Fig. 6g, two peaks (marked with the red symbol) appear at a specific location, which is not observed in the other three figures (Fig. 6d–f). The first peak represents SO_4^{2-} to emphasize that the content of SO_4^{2-} is higher than that of products under other conditions. The second one contributes to CO_3^{2-}. It can be observed from Fig. 6d–g that characteristic peaks of $NaHCO_3$ and Na_2SO_3 are observed, indicating insufficient oxidation. At the same time, the characteristic peak of Na_2CO_3 at $\theta = 56.996$ disappears, while a strong characteristic peak is exhibited here in the samples with NO.

3.3 Influence of different factors on SO_2 removal

The continual growth of the desulfurization efficiency with the increase in SO_2 concentration is depicted in Fig. 7a, and the efficiency (4 of Na2/S) is two times as high as that of 2. This could be attributed to the low probability of collision. In collision theory, the actual reaction rate is decided by the effective collision. The probability of effective collision is determined by two factors: (1) the appropriate path orientation and (2) the number of activated molecules. With the increase in concentration, the number of activated molecules is raised (at a constant temperature, the percentage of activated molecules is not changed), which leads to an elevating reaction rate. A high SO_2 concentration can give rise to a large number of activated molecules. In addition, the increase in Na2/S contributed to the growing probability of the appropriate path orientation. This result shows that the rate-limiting step is SO_2 diffusion into the surface of $NaHCO_3$, which is consistent with the inhibition by CO_2 and the promotion by water vapor.

As shown in Fig. 7b, the temperature of 100–200 °C has a promoting effect on the desulfurization efficiency and is
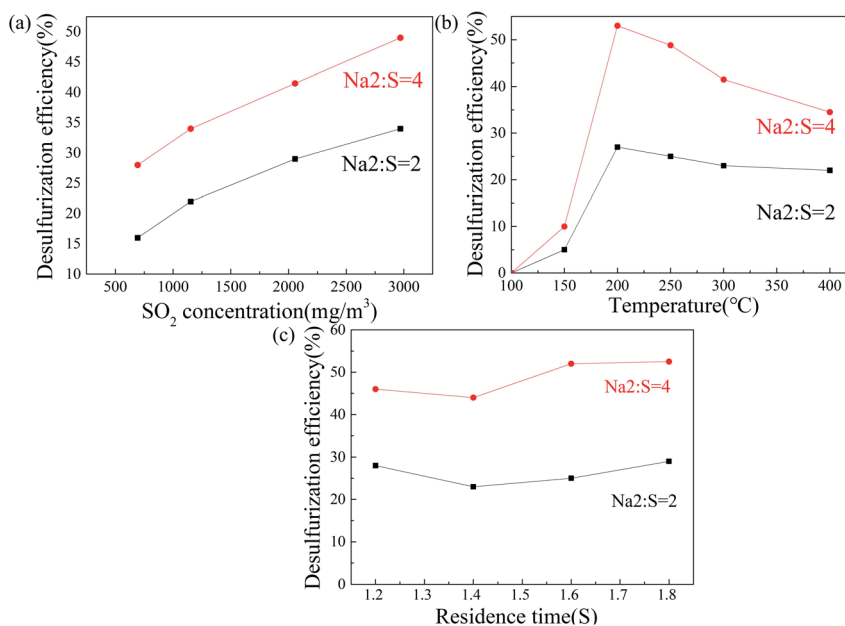

Fig. 7 (a) Effect of SO_2 concentration on SO_2 removal. (b) Effect of temperature on SO_2 removal. (c) Effect of residence time on SO_2 removal (reaction conditions: temperature: inlet temperature of the reaction zone was 220 °C, the outlet temperature of the reaction zone was 180 °C; air volume flow rate: 50 m³ h⁻¹; Na2/S was 2 and 4, respectively; SO_2 concentration: 2000 mg m⁻³).
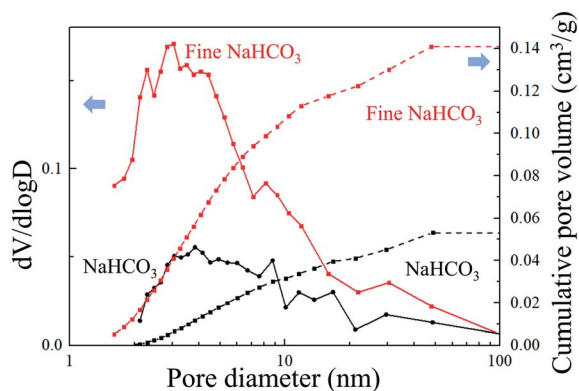
Fig. 8 Differential pore volume *versus* pore size diameter and cumulative pore volume for fine $NaHCO_3$ and $NaHCO_3$.

inhibited at 200–400 °C. $NaHCO_3$ is gradually decomposed from 50 °C. More channels for SO_2 diffusion are exhibited. $NaHCO_3$ at 260 °C is decomposed completely,[52] so the effect of temperature on efficiency is limited. After the temperature reached 300 °C, it was inhibited due to the sintering process. As shown in Fig. 7c, when the Na2/S is 4, the residence time changes from 1.4 s to 1.8 s, and the SO_2 removal efficiency is slightly added from 44% to 52.5%, which is comparable to that used as the Na2/S is 2.

Based on the formula (3)–(5), the draft fan was selected to control the residence time by controlling the air flow rate.

$$Q = 60 \times A \times v \tag{9}$$

Table 2 BET analysis results

Materials	Specific surface area ($m^2\ g^{-1}$)	Adsorption average pore size by BJH method (nm)
Fine $NaHCO_3$	111.04	4.933
$NaHCO_3$	28.435	7.444

$$t = \frac{l}{v} \tag{10}$$

$$A = \pi \times r^2 \tag{11}$$

where Q is the flue gas flow rate, $m^3\ h^{-1}$; A is the pipe cross-sectional area, m^2; v is the flue gas velocity, $m\ s^{-1}$; t is the flue gas residence time in the reaction zone, s; l is the reaction zone length, m; r is the radius of reaction zone pipe, m.

It is worth mentioning that the efficiency is not improved immediately by the increasing residence time, which demonstrates a slight decline at first. It can contribute to the control mode of residence time. The elevation in residence time is not enough to resist the decrease in molecular diffusion due to the lower wind speed. Until the reaction time is long enough, the efficiency is enhanced as expected.

3.4 Effect of the particle size of $NaHCO_3$ on the removal of SO_2

Two different sizes of $NaHCO_3$ were used in the experiment, and the results are shown in Fig. 8.
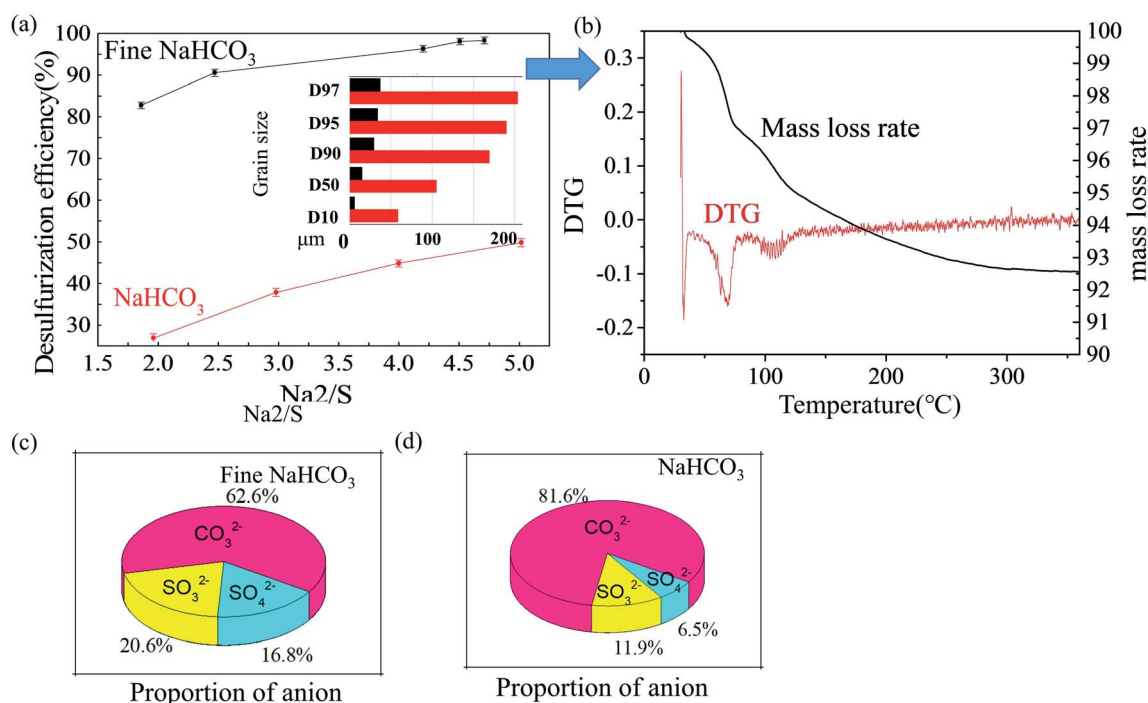

Fig. 9 (a) Desulfurization effect of $NaHCO_3$ and fine $NaHCO_3$ at 200 °C. (b) Thermogravimetric analyses of desulfurization products using fine $NaHCO_3$ (N_2 as a carrier, heating rate: 10 °C min^{-1}, maximum temperature: 800 °C). (c) Content of the desulfurization product of fine $NaHCO_3$. (d) Content of the desulfurization product of $NaHCO_3$ (reaction conditions: temperature: inlet temperature of the reaction zone was 220 °C, the outlet temperature of the reaction zone was 180 °C; air flow rate was kept at 50 $m^3\ h^{-1}$; SO_2 concentration was set at 2000 mg m^{-3}).
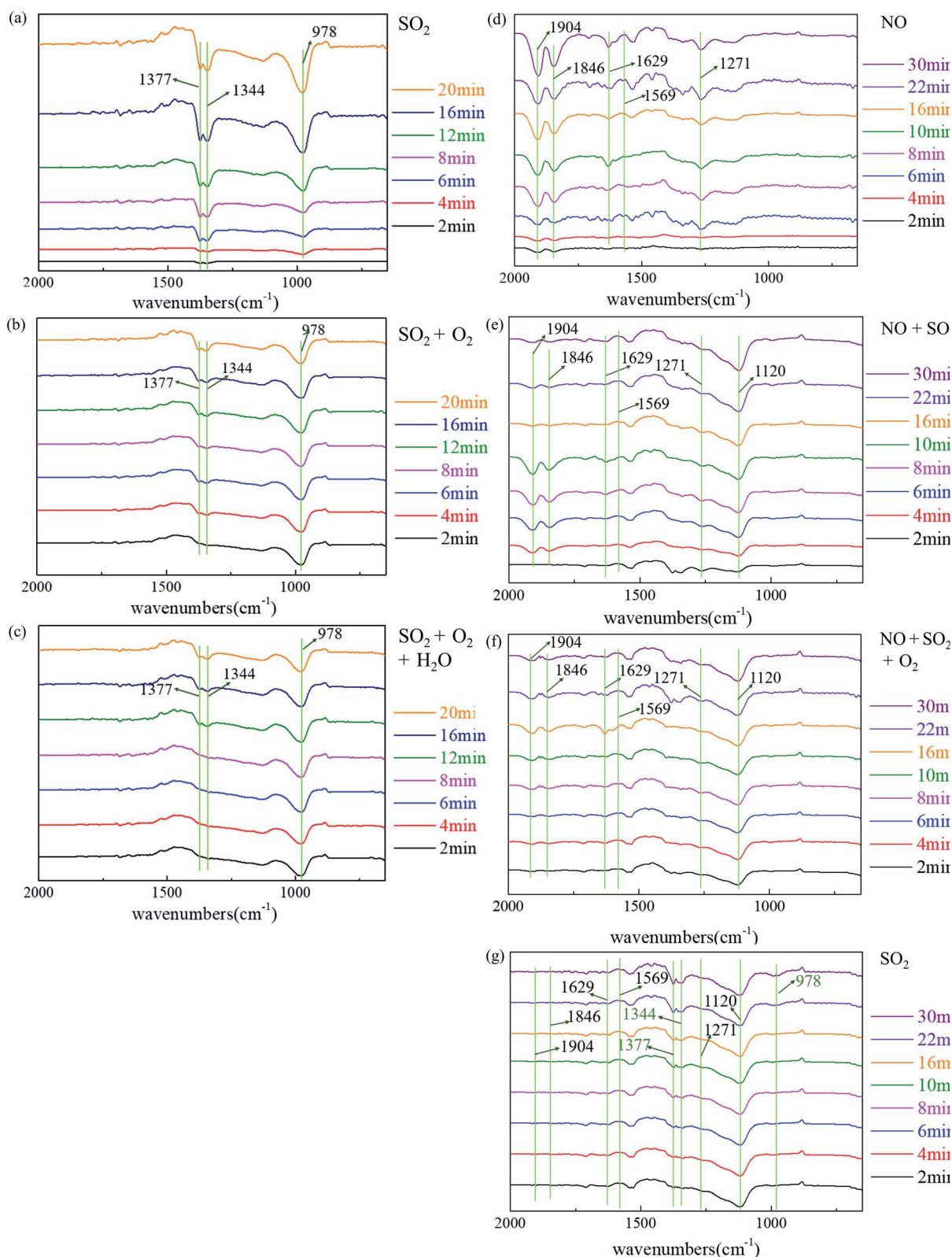
Fig. 10 *In situ* FTIR spectra of (a) 700×10^{-6} SO$_2$ adsorption, (b) 700×10^{-6} SO$_2$ + 21% O$_2$ adsorption and (c) 700×10^{-6} SO$_2$ + 21% O$_2$ + 8% water vapor adsorption on NaHCO$_3$. *In situ* FTIR spectra of (d) 450×10^{-6} NO adsorption, (e) 700×10^{-6} SO$_2$ + NO adsorption, (f) 450×10^{-6} NO + 700×10^{-6} SO$_2$ + 21% O$_2$ adsorption and (g) 700×10^{-6} SO$_2$ on NaHCO$_3$.

BET results of two kinds of $NaHCO_3$ are listed in Table 2, and the pore volume distribution results are depicted in Fig. 8.

Fine $NaHCO_3$ was produced by grinding from $NaHCO_3$. As shown in Fig. 9a, fine $NaHCO_3$ presents better efficiency. In addition, the particle size of fine $NaHCO_3$ is smaller than that of $NaHCO_3$. In addition, a larger volume on fine $NaHCO_3$ is illustrated on the smaller pore parameters than $NaHCO_3$ in Fig. 8, which is beneficial to mixing uniformly with SO_2. In Table 1, it manifests the higher specific surface area of 111.04 m^2 g^{-1} for fine $NaHCO_3$ than that for $NaHCO_3$ of 28.435 m^2 g^{-1}, and the adsorption average pore size is reduced by the BJH method. A similar case researched by Walawska et al.[53] identified similar conclusions that both smaller particle size and larger specific surface area were responsible for the higher conversion and instantaneous efficiency. Fig. 9b shows a weight loss process between 50 °C and 80 °C and a weight loss process between 80 °C and 130 °C. It is known that the first weight loss process is the separation of bound water in the sample. The second one is the decomposition of $NaHCO_3$ with a low utilization rate of $NaHCO_3$. The high utilization of $NaHCO_3$ will be studied next. The high utilization of fine $NaHCO_3$ is proved by Fig. 9c and d.

3.5 Reaction intermediates and mechanism

Fig. 10a–c show the in situ FTIR spectra of SO_2 adsorption at 200 °C under different conditions. Several bands at 1377, 1344 and 978 cm^{-1} are observed, respectively. The band at 978 cm^{-1} represents the stretching vibration of surface-coordinated bisulfite and/or sulfite.[54] The bands at 1377 and 1344 cm^{-1} can be attributed to the asymmetric and symmetric stretching vibrations of SO_2 species combined by chemical adsorption.[55] These results indicate that the participation of oxygen and water vapor has no noticeable effect on the oxidation of SO_2, which is consistent with the experimental results.

Fig. 10d–g shows the in situ FTIR spectra with NO on $NaHCO_3$ at 200 °C under different conditions. After introducing only NO into the IR cell, the bands at 1904, 1846, 1629, 1569 and 1271 cm^{-1} are observed, respectively. These bands at 1904, 1846, 1629 and 1271 cm^{-1} all represent nitrite species,[56–58] while the band at 1569 is assigned to the nitrate species.[59] Notably, after the introduction of SO_2 and NO, the band at 1120 appears, which indicates that sulfate is formed.[60] No obvious bands representing SO_3^{2-} appear. In addition, the bands representing NO almost vanish after 10 min, which indicates a similar evolution process after SO_2, O_2 and NO introduction. After purging with N_2 and only SO_2 introduced, bands at 1120 still exit. Meanwhile, the bands at 1377, 1344 and 978 cm^{-1} appear, which indicates that the formation of sulfate is promoted by NO. In addition, the band at 1569 cm^{-1} does not vanish, illustrating the stable presence of nitrate species, which was proposed above.

4 Conclusions

In summary, desulfurization by $NaHCO_3$ was systematically studied by scale-up experiments. These results indicated that the diffusion of SO_2 into the channel of $NaHCO_3$ was the rate-limiting step. Meanwhile, the role of NO in promoting sulfate formation was confirmed and its reaction mechanism was proposed. Increasing the ratio of sodium to sulfur and the residence time would have a promotive effect on desulfurization efficiency. However, more attention should be paid to material waste and high costs. The efficient utilization of $NaHCO_3$ such as material recycling and the addition of additives to promote the decomposition of sodium bicarbonate will be the next direction. In the practical application process, increasing the flow rate to improve the residence time will be a more effective way. However, due to site constraints, empty tower circulation and other ways can promote the reaction effect. Fine sodium bicarbonate could effectively enhance the reaction rate and improve the desulfurization effect. This work may inspire further development of dry integrated multi-pollutant removal with a clear explanation for different factors on desulfurization.

Author contributions

Shuangchen Ma: revised the manuscript, supervision. Xuan Bie: draft writing and editing. Chunqin Gong: methodology and some experimental data collection. Baozhong Qu: designed some experiments and conducted some characterizations of samples. Daokuan Liu: conducted some characterizations of the samples.

Conflicts of interest

There are no conflicts to declare.

Acknowledgements

References

1 R. L. Hao, Y. M. Mao, X. Z. Mao, Z. Wang, Y. P. Gong, Z. L. Zhang and Y. Zhao, Cooperative removal of SO_2 and NO by using a method of UV-heat/H_2O_2 oxidation combined with NH_4OH-$(NH_4)_2SO_3$ dual-area absorption, Chem. Eng. J., 2019, 365, 282–290.

2 R. L. Hao, X. Z. Mao, Z. Wang and Y. Zhao, A Novel Method of Ultraviolet/$NaClO_2$–NH_4OH for NO removal: mechanism and kinetics, J. Hazard. Mater., 2019, 368, 234–242.

3 Y. Shan, W. Yang, Y. Li and Y. X. Liu, Preparation of microwave-activated magnetic bio-char adsorbent and study on removal of elemental mercury from flue gas, Sci. Total Environ., 2019, 697, 134049.

4 C. Y. Su, R. Xu, J. L. Hu and C. L. Shao, Photocatalytic Process of Simultaneous Desulfurization and Denitrification of Flue Gas by TiO_2-polyacrylonitrile nanofibers, Environ. Sci. Technol., 2013, 47, 11562–11568.

5 Y. Wang, X. Han and Y. X. Liu, Removal of carbon monoxide from simulated flue gas using two new fenton systems:

Mechanism and Kinetics, *Environ. Sci. Technol.*, 2019, **53**, 10387–10397.

6 Q. Zhou, J. X. Yang, M. M. Liu and Y. Liu, Toxicological risk by inhalation exposure of air pollution emitted from China's municipal solid waste incineration, *Environ. Sci. Technol.*, 2018, **52**, 11490–11499.

7 G. Sharma, S. B. Pallavi, H. Hakkim and B. P. Chandra, Gridded emissions of CO, NO_x, SO_2, CO_2, NH_3, HCl, CH_4, $PM_{2.5}$, PM_{10}, BC, and NMVOC from open municipal waste burning in India, *Environ. Sci. Technol.*, 2019, **53**, 4765–4774.

8 J. C. Xu, J. Zhang and Y. Yu, Characteristics of vapor condensation on coal-fired fine particles, *Energy Fuels*, 2016, **303**, 1822–1828.

9 Y. G. Adewuyi and N. Y. Sakyi, Simultaneous absorption and oxidation of nitric oxide and sulfur dioxide by aqueous solutions of sodium persulfate activated by temperature, *Ind. Eng. Chem. Res.*, 2013, **52**, 11702–11711.

10 Q. Wang, Y. Miyake and M. Tokumura, Effects of characteristics of waste incinerator on emission rate of halogenated polycyclic aromatic hydrocarbon into environments, *Sci. Total Environ.*, 2018, **625**, 633–639.

11 Y. Zhao, T. X. Guo and Z. Y. Chen, Simultaneous removal of SO_2 and NO using $M/NaClO_2$ complex absorbent, *Chem. Eng. J.*, 2010, **160**, 42–47.

12 B. Wu and Y. Q. Xiong, A novel low-temperature NO removal approach with ˙OH from catalytic decomposition of H_2O_2 over $La_{1-x}Ca_xFeO_3$ oxides, *J. Chem. Technol. Biotechnol.*, 2018, **93**, 43–53.

13 J. H. Park, J. W. Ahn, K. H. Kim and Y. S. Son, Historic and futuristic review of electron beam technology for the treatment of SO_2 and NO_x in flue gas, *Chem. Eng. J.*, 2019, **355**, 351–366.

14 A. G. Chmielewski, E. Zwolińska, J. Licki, Y. X. Sun, Z. Zimek and S. Bułka, A hybrid plasma-chemical system for high-NO_x flue gas treatment, *Radiat. Phys. Chem.*, 2018, **144**, 1–7.

15 P. Hoffmann, C. Roizard, F. Lapicque, S. Vénot and A. Maire, Process for the Simultaneous Removal of SO_2 and NO_x Using Ce(IV) Redox Catalysis, *Process Saf. Environ. Prot.*, 1997, **75**, 43–53.

16 B. M. Obradović, G. B. Sretenović and M. M. Kuraica, A dual use of DBD plasma for simultaneous NO_x and SO_2 removal from coal-combustion flue gas, *J. Hazard. Mater.*, 2011, **185**, 1280–1286.

17 Y. X. Liu, Y. Shan and Y. Wang, Novel simultaneous removal technology of NO and SO_2 using a semi-dry microwave activation persulfate system, *Environ. Sci. Technol.*, 2020, **54**(3), 2031–2042.

18 X. Zhou, H. X. Yi and X. L. Tang, Thermodynamics for the adsorption of SO_2, NO and CO_2 from flue gas on activated carbon fiber, *Chem. Eng. J.*, 2012, **200–202**, 399–404.

19 Y. Zhao and J. Han, Simultaneous SO_2 and NO removal from flue gas based on TiO_2 photocatalytic oxidation, *Environ. Technol.*, 2009, **30**, 555–1563.

20 J. H. Yoon, H. W. Park and D. W. Park, Simultaneous oxidation and absorption of NO_x and SO_2 in an integrated O_3 oxidation/wet atomizing system, *Energy Fuels*, 2016, **3043**, 289–3297.

21 G. Y. Xie, Z. Y. Liu, Z. P. Zhu and Q. Y. A. Liu, Simultaneous removal of SO_2 and NO_x from flue gas using a CuO/Al_2O_3 catalyst sorbent: II. Promotion of SCR activity by SO_2 at high temperatures, *J. Catal.*, 2004, **224**, 42–49.

22 E. Kowsari and S. Abdpour, Investigation performance of rod-like ZnO/CdO composites, synthesized in ionic liquid medium as photocatalytic for degradation of air pollutants (SO_2 and NO_x), *Optik*, 2016, **127**, 11567–11576.

23 S. P. Cui, R. L. Hao and D. Fu, Integrated method of non-thermal plasma combined with catalytical oxidation for simultaneous removal of SO_2 and NO, *Fuel*, 2019, **246**, 365–374.

24 Y. Yang, R. Whiddon and Z. H. Wang, Investigation of NO removal with ozone deep oxidation in Na_2CO_3 solution, *Energy Fuels*, 2019, **335**, 4454–4461.

25 H. M. Yang, H. Liu and H. Wu, Photochemical removal of gaseous elemental mercury in a dielectric barrier discharge plasma reactor, *Plasma Chem. Plasma Process*, 2012, **32**, 969–977.

26 J. H. Ye, J. Shang, H. Song, Q. Li and T. Zhu, Generation of reactive oxygen species in simulated flue gas under vacuum ultraviolet radiation, *Chem. Eng. J.*, 2013, **232**, 26–33.

27 L. Luo, Y. Y. Guo and T. Y. Zhu, Adsorption species distribution and multicomponent adsorption mechanism of SO_2, NO, and CO_2 on commercial adsorbents, *Energy Fuels*, 2017, **3110**, 11026–11033.

28 Y. J. Li, X. L. Zhang, H. F. Lin, F. Q. Yu, Z. H. Chen, C. M. Li, Z. E. Liu, J. Yu and S. Q. Gao, The simultaneous removal of SO_2 and NO from flue gas over activated coke in a multi-stage fluidized bed at low temperature, *Fuel*, 2020, **275**, 117862.

29 L. Yang, L. Yao, Y. T. Liu, X. Zhao, X. Jiang and W. J. Jiang, Bimetallic and polymetallic oxides modification of activated coke by one-step blending method for highly efficient SO_2 removal, *Energy Fuels*, 2020, **34**, 7275–7283.

30 Z. Hu, H. Zhou, W. Zhang and S. Wu, The influence of the porous structure of activated coke for the treatment of gases from coal combustion on its mechanical strength, *Processes*, 2020, **8**, 900.

31 J. M. Rosas, R. Ruiz-Rosas, J. Rodríguez-Mirasol and T. Cordero, Kinetic study of SO_2 removal over lignin-based activated carbon, *Chem. Eng. J.*, 2017, **307**, 707–721.

32 *ReACT reduces emissions and water use*, https://www.powermag.com/react-reduces-emissions-and-water-use/, 2010, vol. 6, p. 1.

33 B. K. Saikia, A. M. Dutta and B. P. Baruah, Feasibility studies of de-sulfurization and de-ashing of low grade medium to high sulfur coals by low energy ultrasonication, *Fuel*, 2014, **123**, 12–18.

34 X. H. Dong, Z. Wang and Y. Zhao, Elemental mercury removal by a method of ultraviolet-heat synergistically catalysis of H_2O_2 halide complex, *Environ. Sci. Technol.*, 2019, **53**, 8324–8332.

35 B. Wu and Y. Q. Xioang, Enhancement of NO absorption in ammonium-based solution using heterogeneous Fenton reaction at low H_2O_2 consumption, *Korean J. Chem. Eng.*, 2016, **33**, 3407–3416.

36 X. M. Huang, J. Ding and Q. Zhong, Catalytic decomposition of H_2O_2 over Fe-based catalysts for simultaneous removal of NO_x and SO_2, *Appl. Surf. Sci.*, 2015, **30**, 66–72.

37 Y. X. Liu, Y. Wang and Q. Wang, Simultaneous Removal of NO and SO_2 using vacuum ultraviolet light (VUV)/heat/peroxymonosulfate (PMS), *Chemosphere*, 2018, **190**, 431–441.

38 Y. X. Liu and Q. Wang, Novel process on simultaneous removal of nitric oxide and sulfur dioxide using vacuum ultraviolet (VUV)-activated $O_2/H_2O/H_2O_2$ system in a wet VUV-spraying Reactor, *Environ. Sci. Technol.*, 2016, **50**, 12966–12975.

39 R. L. Hao, X. Z. Mao, Z. Qian, Y. Zhao, L. D. Wang, B. Yuan, K. M. Wang, Z. H. Liu, Q. Meng and J. Crittenden, Simultaneous removal of SO_2 and NO using a novel method of ultraviolet irradiating chlorite-ammonia complex, *Environ. Sci. Technol.*, 2019, **53**, 9014–9023.

40 R. L. Hao, Z. Wang, X. Z. Mao, B. Yuan and Y. Zhao, Elemental mercury removal by a novel advanced oxidation process of ultraviolet/chlorite-ammonia: mechanism and kinetics, *J. Hazard. Mater.*, 2019, **374**, 120–128.

41 Y. X. Liu, Y. Wang and Z. Y. Liu, Oxidation removal of nitric oxide from flue gas using UV photolysis of aqueous hypochlorite, *Environ. Sci. Technol.*, 2017, **51**, 11950–11959.

42 S. C. Ma, X. Bie, X. Huang, Y. Sun, K. X. Chen and Z. P. Zhu, Desulfurization experiment analysis based on control of multiple pollutants in flue gas at medium temperature, *Chem. Ind. & Eng. Pro.*, 2017, **37**(S1), 210–217.

43 J. Mareček, K. Mocek and E. Erdös, Kinetics of the reaction between the solid sodium carbonate and the gaseous sulfur dioxide. IV: effect of the gas phase composition and of temperature in an integral Fixed-Bed reactor, *Collect. Czech. Chem. Commun.*, 1970, **35**, 154–164.

44 V. Manovic and E. J. Anthony, Steam reactivation of spent CaO based sorbent for multiple CO_2 Capture Cycles, *Environ. Sci. Technol.*, 2007, **41**, 1420–1425.

45 R. T. Symonds, D. Y. Lu, A. Macchi, R. W. Hughes and E. J. Anthony, CO_2 capture from syngas *via* cyclic carbonation/calcination for a naturally occurring limestone: modeling and bench-scale testing, *Chem. Eng. Sci.*, 2009, **64**, 3536–3543.

46 P. Sun, J. R. Grace, C. J. Lim and E. J. Anthony, An investigation of attempts to improve cyclic CO_2 capture by sorbent hydration and modification, *Ind. Eng. Chem. Res.*, 2008, **47**, 2024–2032.

47 R. H. Borgwardt, Calcium oxide sintering in atmospheres containing water and carbon dioxide, *Ind. Eng. Chem. Res.*, 1989, **28**, 493–500.

48 S. K. Bhatia and D. D. Perlmutter, Effect of the product layer on the kinetics of the CO_2-lime reaction, *AIChE J.*, 1983, **29**, 79–86.

49 D. Mess, A. F. Sarofim and J. P. Longwell, Product layer diffusion during the reaction of calcium oxide with carbon dioxide, *Energy Fuels*, 1999, **13**, 999–1005.

50 V. Manovic and J. E. Anthony, Carbonation of CaO-based sorbents enhanced by steam addition, *Ind. Eng. Chem. Res.*, 2010, **49**, 9105–9110.

51 B. Hou, H. Qi and C. F. You, Dry desulfurization in a circulating fluidized bed (CFB) with chain reactions at moderate temperatures, *Energy Fuels*, 2005, **19**, 73–78.

52 Z. Q. Tan, G. P. Niu, Q. Qi, M. W. Zhou, B. H. Wu and W. Yao, Ultralow emission of dust, SO_x, HCl, and NO_x using a ceramic catalytic filter tube, *Energy Fuels*, 2020, **34**, 4173–4182.

53 B. Walawska, A. Szymanek, A. Pajdak and M. Nowak, Flue gas desulfurization by mechanically and thermally activated sodium bicarbonate, *Polish J. Chem. Technol.*, 2014, **16**(3), 56–62.

54 L. Zhao, X. Y. Li, C. Hao and L. C. Raston, SO_2 adsorption and transformation on calcined NiAl hydrotalcite-like compounds surfaces: an in situ FTIR and DFT study, *Appl. Catal. B-Environ.*, 2012, **117–118**, 339–345.

55 C. Sun, N. Zhao, Z. Zhuang, H. Wang, Y. Liu, X. Weng and Z. Wu, Mechanisms and reaction pathways for simultaneous oxidation of NO_x and SO_2 by ozone determined by *in situ* IR measurements, *J. Hazard. Mater.*, 2014, **274**, 376–383.

56 C. D. Craver, *The coblentz society desk book of infrared spectra*, DTIC document, 1977.

57 H. M. Wang, P. Ning, Y. Q. Zhang, Y. P. Ma, J. F. Wang, L. Y. Wang and Q. L. Zhang, Highly efficient WO_3–FeO_x catalysts synthesized using a novel solvent-free method for NH_3-SCR, *J. Hazard. Mater.*, 2020, **388**, 121812.

58 J. Fan, P. Ning, Y. C. Wang, Z. X. Song, X. Liu, H. M. Wang, J. Wang, L. Y. Wang and Q. L. Zhang, Significant promoting effect of Ce or La on the hydrothermal stability of Cu-SAPO-34 catalyst for NH_3-SCR reaction, *Chem. Eng. J.*, 2019, **369**, 908–919.

59 L. Lietti, M. Daturi, V. Blasin-Aubé, G. Ghiotti, F. Prinetto and P. Forzatti, Relevance of the Nitrite Route in the NO_x Adsorption mechanism over Pt-Ba/Al_2O_3 NO_x storage reduction catalysts investigated by using operando FTIR spectroscopy, *ChemCatChem*, 2011, **4**, 55–58.

60 S. F. Weng, *Fourier transform infrared spectroscopy analysis*, Chemical Industry Press, China, 2010.